# Nanomechanical Silicon Resonators with Intrinsic Tunable Gain and Sub-nW Power Consumption

**Sebastian T. Bartsch, Andrea Lovera, Daniel Grogg, and Adrian M. Ionescu***

Nanoelectronic Devices Laboratory, Ecole Polytechnique Fédéral de Lausanne (EPFL), 1015 Lausanne, Switzerland

**ABSTRACT**

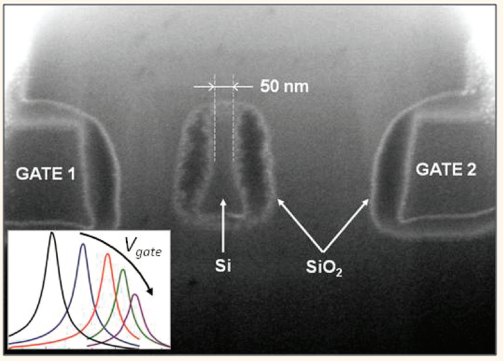


Nanoelectromechanical systems (NEMS) as integrated components for ultrasensitive sensing, time keeping, or radio frequency applications have driven the search for scalable nanomechanical transduction on-chip. Here, we present a hybrid silicon-on-insulator platform for building NEM oscillators in which fin field effect transistors (FinFETs) are integrated into nanomechanical silicon resonators. We demonstrate transistor amplification and signal mixing, coupled with mechanical motion at very high frequencies (25—80 MHz). By operating the transistor in the subthreshold region, the power consumption of resonators can be reduced to record-low nW levels, opening the way for the parallel operation of hundreds of thousands of NEM oscillators. The electromechanical charge modulation due to the field effect in a resonant transistor body constitutes a scalable nanomechanical motion detection all-on-chip and at room temperature. The new class of tunable NEMS represents a major step toward their integration in resonator arrays for applications in sensing and signal processing.

**KEYWORDS:** nanoelectromechanical systems · nanotechnology · mixing · silicon-on-insulator · transistor

Nanoelectromechanical systems (NEMS) offer great potential in the field of science and technology. Anticipated as integrated frequency clocks and timing reference,[1] ultralow power digital switch and memory,[2] analog mixer filters,[3] ultrasensitive mass sensors,[4] or as force and charge detectors[5,6] their applications remain versatile. They also represent powerful tools to address fundamental questions in science such as the macroscopic quantum state control,[7] the coupling of mechanical with optical degrees of freedom,[8] or the detection of quantized mechanical motion in mesoscopic systems.[9] For many practical applications, a large-scale integrable transduction scheme remains stringent to realize discretely addressable NEM arrays along with a fabrication process facilitating the NEM interface with readout electronics. However, developing integrated motion detection of submicrometer resonators in the very high frequency (VHF) range at room temperature and with low power dissipation remains a central challenge for future sensor arrays[10] and has been room for substantial scientific innovation over the past decade.

A multitude of motion detection techniques has been implemented: magnetomotive transduction,[11] piezoelectric detection,[12] optical methods including free-space and fiber-optical interferometry,[13] near-field optical techniques,[14] or recently photonic transduction.[15] Generally, optical detection techniques require external instrumentation jeopardizing on-chip readout, and photonic integration implies formidable fabrication difficulties for dimensions down to a few tens of nanometers. Purely capacitive transduction schemes severely suffer of very low signal levels and parasitic feed through at VHF from the device input to output terminals.[16] Still, promising efforts have been reported toward optical multiplexing techniques,[17] and thin film piezoelectric materials have been reported as efficient nanoscale actuators.[18]

As a scalable transducer, intrinsic amplification mechanisms such as piezoresistive read-out or transistor based charge modulation are promising at room temperature. Microwave performance has been demonstrated with piezoresistive bulk mode resonators.[19,20] Large gauge factors in silicon nanowires have been reported for both bottom-up[21] and top-down[22] architectures.

* Address correspondence to adrian.ionescu@epfl.ch.

Received for review September 13, 2011 and accepted December 10, 2011.

**Published online December 11, 2011**
**10.1021/nn203517w**

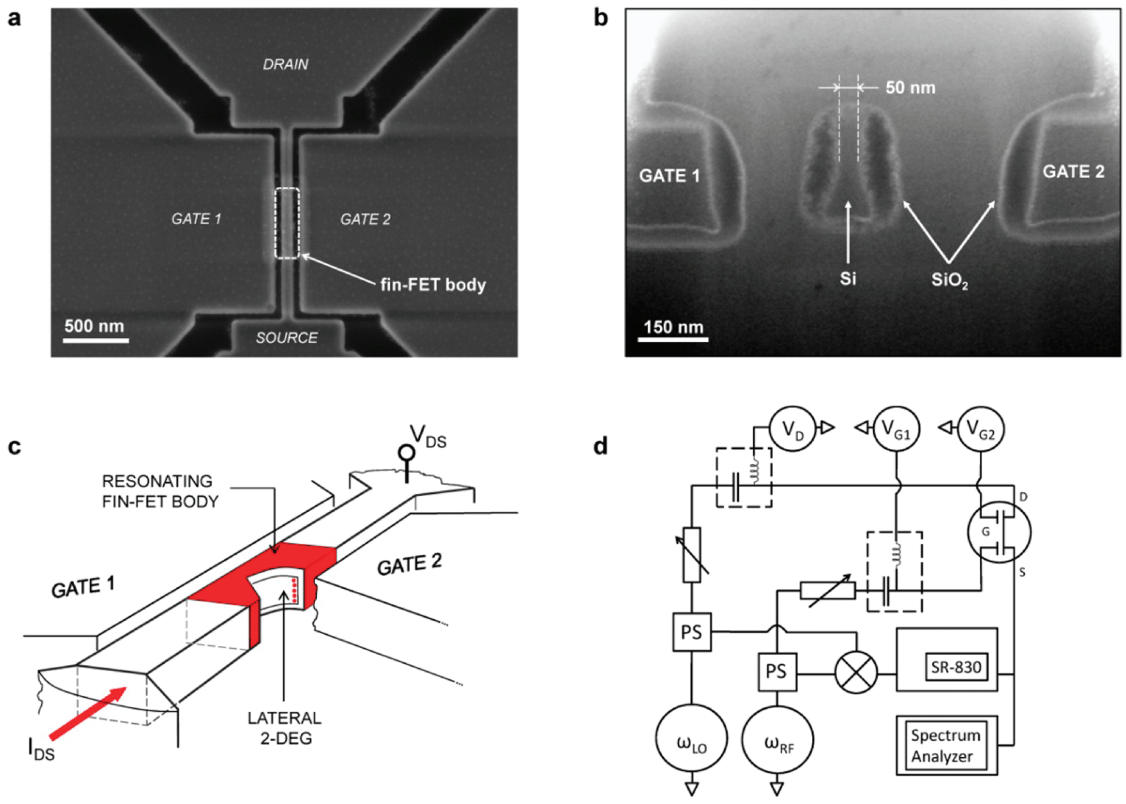


**Figure 1. Nanoelectromechanical resonators with intrinsic transistor self-detection. (a) SEM image showing a clamped–clamped beam with the suspended transistor-body indicated. (b) Cross-sectional SEM image after a focused ion beam cut (FIB) at the center of the beam resonator. The graph shows the resonator prior to the final release of the amorphous silicon mask layer. (c) Working principle of resonant-body transistors. The device is actuated laterally *via* gate electrodes, and the mechanical resonance is monitored *via* the drain current signal. (d) Schematic of the experimental setup for 2-port mixing measurements with RB-FETs with two independent gates. Two signal sources are routed to the device under test and to a reference mixer *via* power splitters (PS), attenuators, and bias-tees. The device output is monitored with a lock-in amplifier (SR-830) at the reference frequency or directly with a spectrum analyzer.**

## DEVICE OPERATING PRINCIPLES

Here, we present a self-transducing NEM system based on the cointegration of a nanowire transistor on suspended silicon resonators. The fabrication is based on a top-down, large-scale CMOS compatible process. Each single device disposes two independent, lateral electrodes which act both as mechanical actuator and transistor gate electrode (input transducer). The mechanical motion is detected by monitoring the output current of the resonant-body (RB) FinFET (output transducer). The suspended transistor, hence, acts as an intrinsic signal amplifier or frequency converter whose properties will depend on bias conditions and design of the transistor itself. We are able to characterize fundamental resonances up to 165 MHz of flexural beam resonators with cross-sectional dimensions tailored from 140 to 400 nm width and several micrometers lengths in both direct scattering parameter and frequency down-mixed measurement schemes. These unique properties allow to further explore the performance of the hybrid transistor-resonator as function of the FET operating point, opening an unprecedented trade-off between available signal gain and dissipated power. Although a great number of materials have been introduced in the domain of NEMS,[4,12,37,38] the presented results show once again the versatility of silicon technology consolidating its preeminent position in micro- and nanoelectronics. In fact, the hybridization of solid state devices and circuits with NEM structures harbors a multitude of new functionalities.

The NEM structure is surface nanomachined from a 4″ silicon-on-insulator (SOI) wafer topped with a 200 nm thin single crystalline silicon. The device layer is initially p-doped at $5 \times 10^{16}$ cm$^{-3}$ (Boron), which later defines the doping concentration of the transistor channel. The channel is located symmetrically around the center of the beam (*i.e.*, around maximum displacement). Separated by narrow air gaps (~100 nm), the latter is electrostatically driven into motion by adjacent gate electrodes (Figure 1a). The mechanical architecture is defined by e-beam lithography, followed by a release-etch of the buried oxide (BOX). The FET is designed to work as a n-channel enhancement mode device with a channel width of ~200 nm, corresponding to the SOI thickness. With the applied electrical field, an inversion charge is created laterally at the silicon/silicon dioxide interface of the resonator. In RB-FinFET devices, the beam oscillation acts directly

on the transistor charge. The drain current, which carries the mechanical properties of the resonator, is modulated directly proportional to the position of the beam. This is to be seen in contrast to conventional capacitively detected MEMS, in which the output current is proportional to the time-derivative with regard to the position of the beam.[23,24]

After BOX release, the suspended NEM device is thermally oxidized (Figure 1b). This provides (i) an interface with low defect density for the electron sheet charge, (ii) a passivation layer minimizing leakage currents through the structure, and (iii) robustness toward back-end functionalization steps envisioned for future NEM-array based gas- and biosensing.[25] The FinFET channel is defined in an $n+$ implantation step (Phosphor) using e-beam structured amorphous silicon layer as hard mask (see Methods and Supporting Information). The maximum depletion depth of the transistor body is roughly $W_{d,max} \sim 150$ nm. Given a body depth of ~50 nm (see Figure 1b), the transistor fins can be fully depleted through the lateral electric field of the gate electrodes, similar to the solid-state counterpart of a fully depleted double-gate MOSFET. The channel is oriented along the ⟨110⟩ axis (the direction of the highest electron mobility in silicon) and is designed at all times shorter than the vibrating beam. Our TCAD simulations suggest a final channel length of $L_{ch} \sim 1\ \mu$m, which we found to be the lower bound for short channel effects in this transistor design. A scaling of the channel length is feasible by improving the doping profile or electrostatic control of the channel, for example, by reducing the gap size with atomic layer deposition of high-k dielectric materials.[26]

As can be inferred from Figure 1c, an inversion charge (2-dimensional electron gas, 2-DEG) may be created at both lateral interfaces. Having both inversion channels "on", the motional current will have two contributions, however, opposite in phase. This leads to an overall zero change in total conductance. To observe the resonance at its excitation frequency, the gate bias is applied asymmetrically throughout this work with one interface in accumulation mode gated with a voltage well below threshold. We apply the RF excitation on the back-gate (constant value) $V_{G1} = V_{G1}^{dc} + \tilde{v}_{g1} \cos \omega t$, which simultaneously allows us to decouple RF excitation force from the transistor bias point set by $V_{G2}$. This is unique for the device architecture presented in this work.

## STATIC CHARACTERISTICS

We investigated the effect of the back-gate bias on the RB-FinFET threshold voltage ($V_{th}$; Figure 2a,b). The threshold voltage has been extrapolated linearly at maximum transconductance for a NEM-device and plotted *versus* the back-gate bias, here $V_{G1}$. Similar to solid-state, fully depleted SOI devices, we observe a "body effect", that is, $dV_{th2}/dV_{G1}$ being constant.[27] The tunable threshold voltage is a significant asset in circuit design and allows to precisely set the point of operation and, hence, compensating fabrication fluctuations of FinFET parameters. Although designed to have a positive threshold voltage, the FinFET transfer characteristics reveal a normally on enhancement mode transistor. The $V_{th}$ shift to lower values is likely caused by charges in/on the gate oxide during process fabrication. Previous work on accumulation NEM devices,[28] enhancement-mode SG-FETs, and dielectric transduction resonating transistors[2,19] show poor subthreshold leakage. Here, clear exponential dependence of $I_D$ on $V_G$ in the weak inversion region with pA off-current levels is achieved, allowing its exploration at resonance. The subthreshold slope is found 400 mV/decade, a value acceptable for air-gap transistors considering an equivalent dielectric thickness EOT about 500 nm. The NEM devices as shown in Figure 1a,b reach transconductance values of 3.5 $\mu$S/$\mu$m and current densities of 15 $\mu$A/$\mu$m, resulting in two-terminal drain-source resistance (contact resistance included) in the order of 100 kΩ (Figure 2c,d).

## RESONANT CHARACTERISTICS

As sensitive motion detection, we exploit the intrinsic properties of the hybrid device. In common-source configuration, the transistor implies signal gain and self-amplifies its own mechanical motion. This allows transmission measurements of submicrometer VHF resonators directly on a vector network analyzer (VNA, in the $Z_0 = 50\ \Omega$ environment) without any additional impedance matching or feed-through cancellation techniques. Figure 3a shows the *S*-parameter transmission ($S_{21}$) on a 70 MHz beam resonator. The unmatched impedance conditions do not reflect the actual available power gain compared to the measured gain of 16 dB. In a 50 Ω matched network, we can expect the power gain to be by 27 dB higher.

To increase measurement sensitivity, the mixing technique is frequently used as scheme for detecting nanomechanical displacement. It relies on the transfer nonlinearities inherent to the device such as the nonlinearity of the electrical field with the force,[29] nonlinear charge-voltage,[30] or current−voltage characteristics, for example, in a NEM-diode.[31] We can further classify homodyne and heterodyne mixing. In homodyne mixing the device output will create a dc component, which corresponds to a rectification of the harmonic input signal. Because it is directly related to its RF properties, this approach is used to study the frequency response of carbon nanotubes (CNTs)[32−35] or single electron transistors.[36] In a heterodyne mixer, the output frequency of interest is a linear combination of input frequencies. It is particularly attractive for NEMS detection, because the low-frequency output

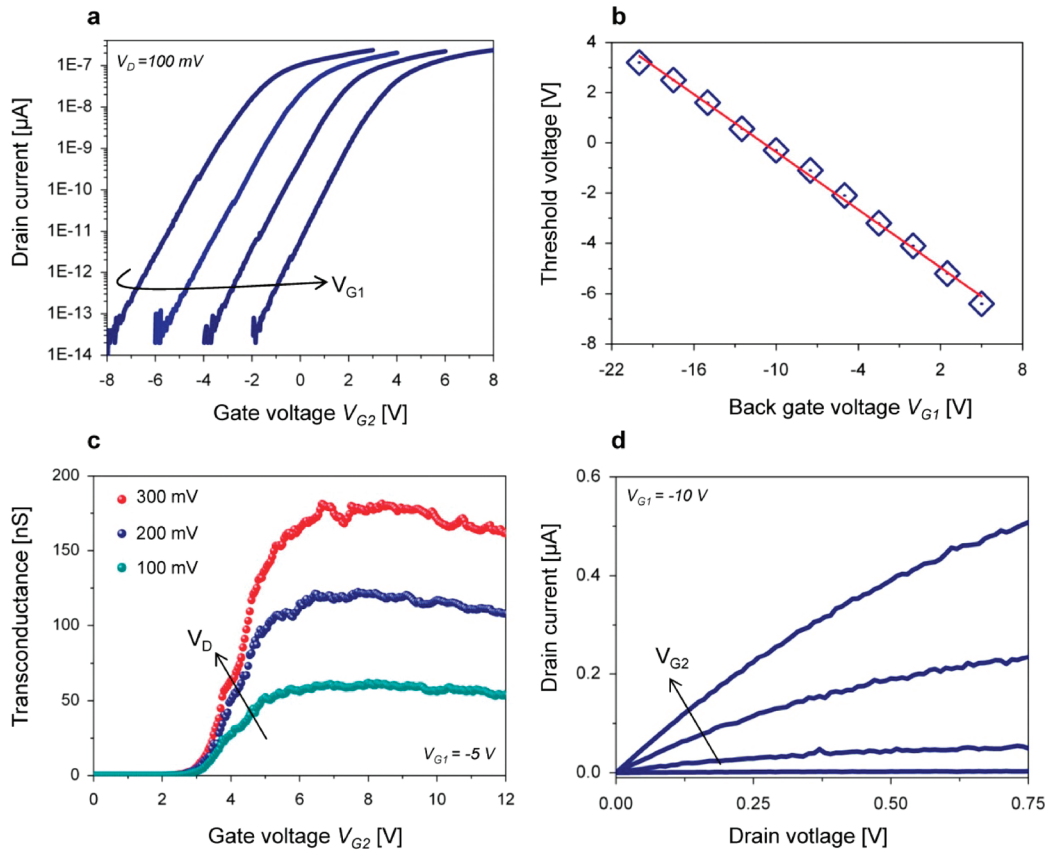


**Figure 2. Static characteristics of FinFET resonators. (a) The transfer curves $I_D$ ($V_G$) are shown with the back-gate voltage $V_{G1}$ = −20, −15, −10, and −5 V as parameter. The drain current exhibits very low off-levels (sub-pA) and clear exponential dependence in weak inversion. (b) The threshold can be tuned with the back-gate voltage from negative to positive values, showing a linear relation. (c) The device transconductance $g_m$ plotted *vs* the gate voltage. The decrease in $g_m$ due to the field induced mobility reduction becomes apparent at higher drain voltages. (d) The output characteristics $I_D$ ($V_D$) are plotted with $V_{G2}$ = +8, 9, 10, and 11 V as parameter, demonstrating linear and saturated FET operating regions.**

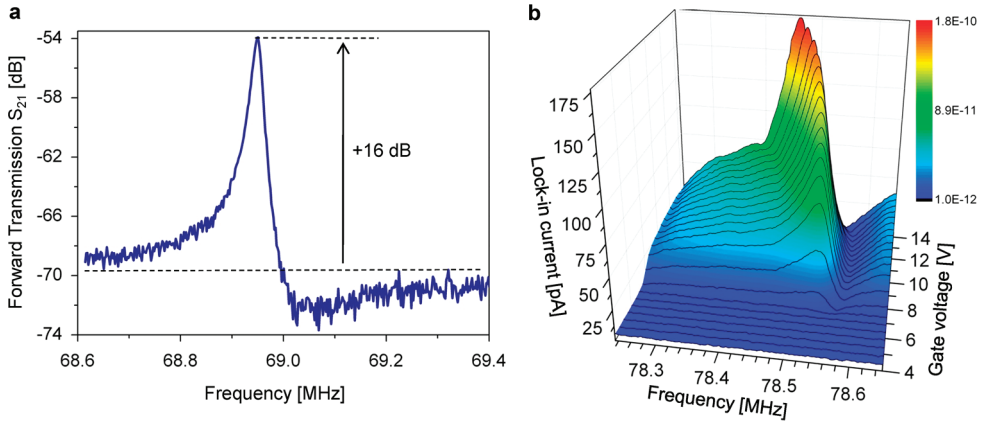


**Figure 3. Spectral response of very high frequency FinFET resonators. (a) Direct scattering-parameter measurement of the transmission coefficient $S_{21}$ of a 70 MHz device ($W_b$ = 400 nm and $L_b$ = 6 $\mu$m), exhibiting 16 dB signal-to-background separation at resonance, a *Q*-factor of 2900 and an extracted motional impedance of $R_m$ = 34 kΩ (high vacuum). The active resonator is biased at $V_{G1}$ = −20 V, $V_{G2}$ = +10 V, $V_D$ = 3 V with a drive power at $P_{ac}$ = −26 dBm. (b) Evolution of the detected signal around resonance as function of the gate voltage from weak to strong inversion using integrated transistor down-conversion. The back-gate is biased at $V_{G1}$ = −10 V. The clamped−clamped beam is 200 nm thick, 150 nm wide, and 3 $\mu$m long, exhibiting a quality factor of ∼1100 (high vacuum).**

component will carry the RF properties of a resonating element and, hence, bypasses the common problems with nanoscale structures, primarily low signal-to-noise ratios related to the massive impedance mismatch, and parasitic in-to-output coupling. This concept has been demonstrated for CNT and, recently, also, graphene-based nanomechanical resonators.[37−39] To provide frequency conversion in FinFET resonators, we exploit

the two device terminals and use the suspended enhancement-mode FET as a *resistive* mixer. In this mode of operation, a local oscillator (LO) signal is applied to the drain, the RF signal to the gate; the intermediate frequency (IF) is filtered from the source (Figure 1d). Note that no dc drain bias is used and the transistor is therefore operated in its linear region, in contrast to a traditional transistor-based amplifier. At low drain-to-source (ac-) voltages, the transistor channel operates as a time-varying resistance. Interestingly, a time-varying element for mixing is, hence, created without using an intrinsic device nonlinearity. Because the linearity channel's resistance is very good, such FET resistive mixers provide generally very low distortion (low spurious mixing) and low Flicker noise, as it has been the first time demonstrated by Maas *et al.*[40] This makes the RB-FET attractive for integrated RF mixer-filter applications. It is emphasized that this mode of operation presented here is different from results reported in,[32−35,41,42] in which the mixing output is given by higher-order terms and proportional to the derivate of the output conductance or transconductance as a consequence of the intrinsic nonlinear source-drain $I_{DS} = f(V_{DS})$ or gate-drain $I_{DS} = f(V_{GS})$ relationship, respectively.

Figure 3b shows the response of a nanomechanical clamped−clamped beam resonator, where the down-converted signal is plotted *vs* frequency and the transistor gate voltage. The RB-FinFET is 140 nm wide, 200 nm thick, and 3 $\mu$m long and resonates in-plane in its ground mode at ∼80 MHz, with a quality factor $Q \sim$ 1100. Note that these are the beam dimensions, in contrast to the active (current carrying) area of the silicon body which has a cross-section of only ∼50 × 200 nm$^2$. The resonance is lower than initially designed ($\omega_0^{Si}/2\pi$ = 170 MHz) using Euler-Bernoulli theory, but agrees fairly well (∼12%) with a stress-dependent resonance frequency[43] and a resulting compressive stress of $-15 \times 10^8$ Nm$^{-2}$, in agreement with values reported in thermal silicon dioxide.[44] For strong inversion operation, these active nanowire resonators provide a 60 dB increase in signal strength at resonance, taking the elastic Duffing instability as upper and the rms of the readout noise as lower limit (see Supporting Information). We highlight the additional gain (hence, dynamic range) delivered by the integrated transistor, which will directly improve phase noise performance in integrated oscillators for applications in high-resolution mass sensing and frequency reference clocks. With an effective mass of $M_{eff} \sim$ 165 fg and a practical dynamic range of ∼40 dB such resonator may offer a mass resolution[4] of $1 \times 10^{-18}$ g at ambient pressure (measured quality factor in air ∼170). In fact, recent work[10,45,46] indicates that nanoscale resonators are more suited toward ambient pressure operation compared to microscale beams.

For hybrid NEM-FET devices, the overall device characteristics result from coupled electrical and mechanical properties of the transistor and resonator, respectively. By comparing the static device characteristics with the mixing output obtained on- and off-resonance, we can validate the mixing principles derived in the following. We consider a two region approach for transistor operation. In strong inversion ($V_G > V_{th}$) and for small $V_D \ll (V_G - V_{th})$, we find ourselves in the linear transistor regime.[47] Assuming harmonic excitations at $\omega$ and $\omega + \omega_{IF}$ and considering only linear terms in the expansion of the drain current, we find the intermediate mixing output at $\omega_{IF}$ away from mechanical resonance to follow the expression

$$\tilde{i}_{IF}^{static} \propto \frac{K}{2}\tilde{v}_d \cdot \tilde{v}_g = \frac{1}{2}\cdot \tilde{g}_m \cdot \tilde{v}_g = \frac{1}{2}\cdot \frac{\partial g_{DS}}{\partial V_G}\tilde{v}_d \cdot \tilde{v}_g \qquad (1)$$

where the transistor constant is $K = (W_{ch}/L_{ch})\mu_n C_{tot}$, $\tilde{v}_d$, and $\tilde{v}_g$ correspond to the harmonic small-signal rms excitation amplitudes at drain and gate, respectively, $g_m$ to the transconductance and $\tilde{g}_m$ to its drain-induced small-signal variation, and $g_{DS} = W/L \cdot \mu_n(\varepsilon) \cdot C_{tot} \cdot (V_G - V_{th})$ the channel output conductance. The total capacitance $C_{tot}$ is approximately $C_{tot} \cong C_{eot}$, where $C_{eot}$ is the equivalent insulator (oxide and air-gap) capacitance. A possible piezoresistive contribution to the drain output signal is taken into account by the strain-dependent electron mobility $\mu_n(\varepsilon)$ in the FET inversion channel.[48]

The channel conductance will be a function of the FET point of operation, that is, of the gate voltage $V_G$ and of the frequency-dependent mechanical displacement $y(\omega)$. At resonance, an additional term arises which can be qualitatively interpreted as a modulation of the threshold voltage (varying capacitance) due to a varying gap under constant biasing conditions. The motional term becomes

$$\tilde{i}_{IF}^{motional} \propto \tilde{g}_m^{\Delta} = \tilde{g}_m \cdot \frac{\varepsilon_{r,ox}}{\varepsilon_{r,ox} t_{gap} + 2t_{ox}} y(\omega) \cdot V_G \cong \tilde{g}_m \cdot \frac{y(\omega)}{t_{gap}} \cdot V_G \qquad (2)$$

where $\tilde{g}_m^{\Delta}(V_G)$ is understood as the additional transconductance available due to the displacement of the beam. The symbol $\varepsilon_{r,ox}$ is the dielectric permittivity of silicon oxide, $t_{ox}$ is the oxide thickness, and $t_{gap}$ is the gap distance. The total current modulation is, hence, the superposition of both contributions. Strikingly, eq 2 reveals that the amplification factor $y(\omega)/t_{gap} \times V_G$ is limited only by mechanical nonlinearity and the maximum amplitude before pull-in occurs. This is a unique feature of the presented novel displacement transducer and a direct result of the intrinsic, electromechanical transistor amplification. In this work, the bias conditions were set far away from pull-in voltages ($V_{pi} > 50$ V). The use of the lock-in amplifier (Stanford Research SR830) necessitates the use of an intermediate frequency (IF) below 100 kHz. Intermediate frequencies (up to 100 MHz)

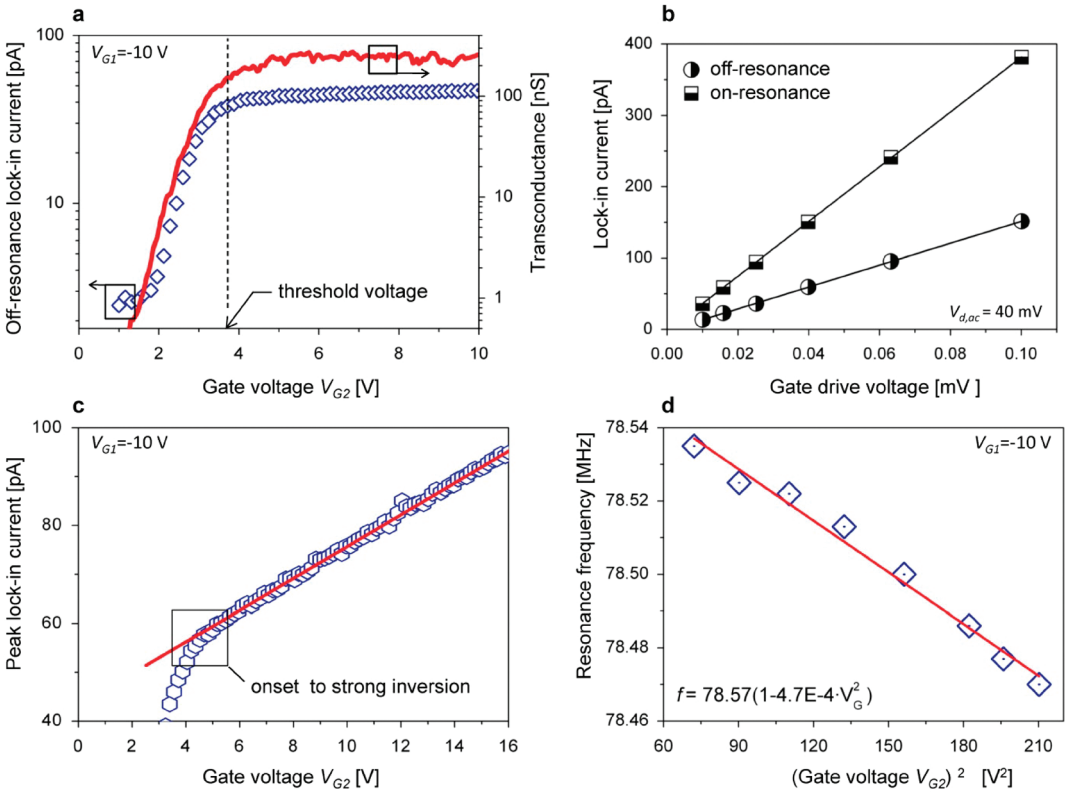


**Figure 4. Correlation of electrical and mechanical properties of FinFET resonators. (a) Correlation of the FET static transconductance (red, $V_D$ = 200 mV) with the mixing output away from resonance (blue). The FET is operated as resistive mixer, biased from weak to strong inversion. (b) The intermediate output at $\omega_{IF}$ relates linearly with the RF-drive amplitudes on- and off-resonance for operation in strong inversion ($V_d^{ac}$ = 10−100 mV). (c) The peak signal at resonance (blue) varies linearly (red line) with the dc bias in strong inversion ($V_d^{ac}$ = 40 mV and $V_g^{ac}$ = 25 mV). (d) The frequency tuning of a nanomechanical resonator shows expected quadratic dependence on the dc bias due to spring softening effect.**

over a wide range of input frequencies were measured directly with the spectrum analyzer (Agilent 89600S). Evidently, this opens up new opportunities of resonant-body transistors as RF-mixer-filter applications on optimized mixer designs, which are sought-after elements, for example, in intermediate heterodyning stages of communication receiver systems. We point out that the mixer operation may be extended to an active scheme in which the RB-FinFETs are operated as square-law mixer (*i.e.*, in saturation $I_D \sim V_G^2$). Providing transconductance, such active FET mixers can offer conversion gain and noise figures superior to passive schemes.[40]

In weak inversion ($V_{G2} < V_{th}$), the drain current varies exponentially with $V_{G2}$. Expanding the expression for the subthreshold current using Taylor series, we find the component at the difference frequency $\omega_{IF}$ to follow:

$$\tilde{i}_{IF,\,sub}^{static} \propto \frac{1}{2}\tilde{v}_g \cdot \tilde{v}_d \cdot \exp V_{G2} \qquad (3)$$

We expect the mixing output to scale with an exponential prefactor $V_{G2}$, which can be clearly inferred from Figure 4a. The trend downward for decreasing gate voltage is essentially limited by the detection noise floor in the preamplifier stage of the lock-in detector. In strong inversion ($V_{G2} > V_{th}$), at several MHz off-resonance, the lock-in signal is quasi-constant with respect to $V_{G2}$, in accordance to the constant transconductance $g_m \propto (W/L)\mu_n(\varepsilon_l)C_{tot}V_D$ of the transistor in linear operation (at low $V_D$).

The bias and drive dependence is summarized in Figure 4b,c. It shows a linear relation with the dc voltage $V_{G2}$ and a linear relation with the RF and LO drive amplitudes. Both are a direct consequence from eqs 1 and 2 and the fact that the driving force term at $\omega_0$ is proportional to $F_{el}^{\omega_0} \propto V_G^{dc}V_G^{ac}\cos\omega_0 t$. This coherently validates the above presented mixing principles. The electrostatic actuation of the resonator provides a gate voltage tuning of the resonance frequency. The dispersive relation $f_0(V_G)$ follows the quadratic relation $k_m \propto f_0^2$, as seen in Figure 4d, where $k_m$ is the mechanical spring constant.

## DISCUSSION

In contrast to passive NEM devices, active resonators consume static power and therefore offer additional trade-off between signal strength and power consumption. In the presented devices, the design of the integrated RB-FinFET can be optimized toward high transconductance or toward low power consumption. Arrays of thousands of resonators envisioned to increase the capture cross-section in sensors will substantially

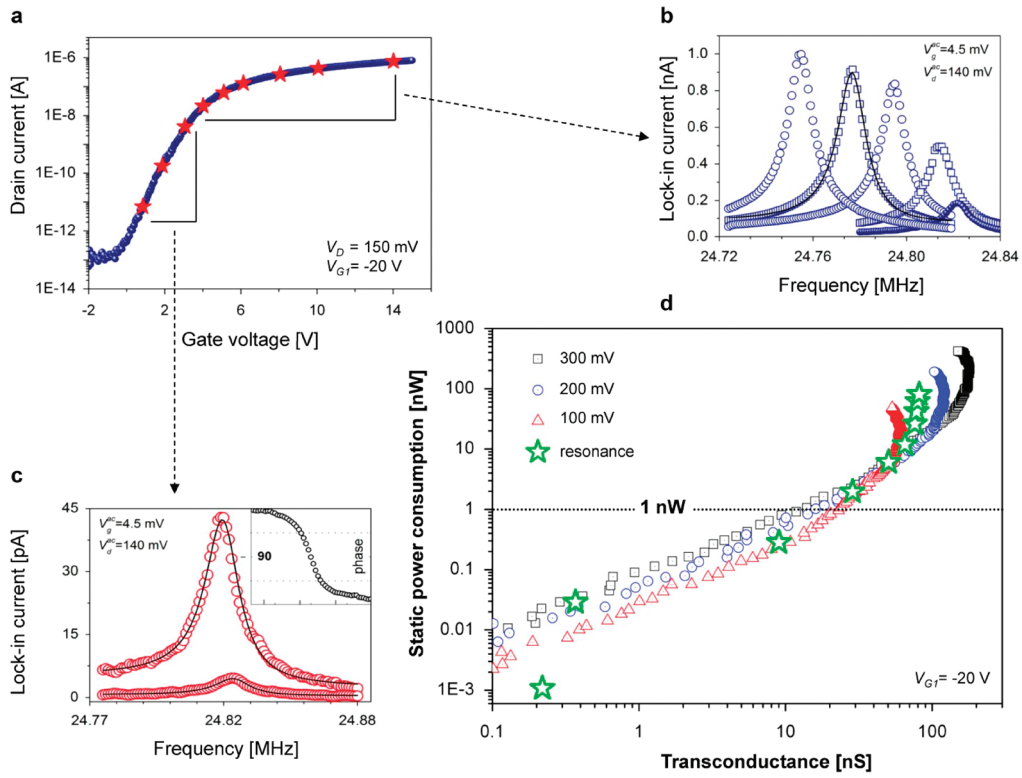


**Figure 5. Unprecedented design space for ultralow power NEM-CMOS systems: accessing nW power consumption in VHF nanomechanical resonators. (a) The transfer characteristics for a 25 MHz resonator ($W_b$ = 400 nm, $L_b$ = 8 $\mu$m) with the different operating points ind icated. The red stars along the transfer curve denote the bias conditions at which the mechanical resonance is later observed. (b) Resonant peaks for decreasing transistor gate bias in strong inversion. (c) The device response in subthreshold for $V_{G2}$ = 3, 2, and 1 V. For consistency, the drive amplitudes were set constant at $V_g^{ac}$ = 4.5 mV and $V_d^{ac}$ = 140 mV in all bias points. The inset shows the associated phase response, indicating the 180° degree phase shift around resonance. (d) The double-log plot illustrates the trade-off opening up between power consumption and available transistor gain. The drain voltage appears as parameter. In strong inversion (and linear operation), the dissipation varies strongly with $V_G$, but with almost constant gain, while in weak inversion the gain and consumption are exponentially traded off.**

increase on-chip power consumption. Reduced power consumption close to or in subthreshold is therefore of great interest for LSI systems. The previous analysis allows us to precisely correlate the RB-FinFET as mixer with the respective static point of operation. This is significant as we can now estimate the power consumption of resonant transistors encountered in their final application, that is, as active device interfaced with on-chip oscillator circuitry. To demonstrate the unique tunability of RB-FinFETs, we take a 400 nm wide and 8 $\mu$m long beam resonator. Figure 5a shows the transfer characteristic of the RB-FinFET. The resonances at 25 MHz in strong to moderate inversion are displayed for several values of $V_{G2}$ in Figure 5b. Figure 5c shows the spectral response of the resonator for the gate voltages at $V_{G2}$ = 3, 2, and 1 V, which correspond to deep subthreshold operation. These findings open a design space between gain and static power consumption which is manifested in Figure 5d as double-logarithmic plot. In strong inversion, the dc consumption varies considerably with the drain voltage (right half of the graph) and reaches a level of tens of $\mu$W. In the region of the weak inversion it is becomes possbile to operate the FinFET resonators with dc consumptions well below tens of nW, down to pW range.[49] The resonance values are evaluated at a chosen drain bias of $V_{DS}$ = 150 mV. Because the resistive mixer measurement is correlated to $V_G$, but not to $V_{DS}$, any other drain voltage value could be picked for Figure 5c. However, due to the weak dependence of $V_{DS}$ on $I_{DS}$ in weak inversion for $V_{DS}$ > 3 kT in an optimized FET design, the core idea communicated of reaching nW-power consumption levels in moderate-to-weak inversion holds. In previous active MEM resonators,[19,20,23,28] the dc power consumption was found to be dominant over the ac one, ranging from 100 $\mu$W to 10s of mW (compare to typical $P^{ac} \lesssim -20$ dBm = 1 $\mu$W). Here, we obtain 3 orders of magnitude of $g_m$ *versus* 6 orders of magnitude in $P^{dc}$ values offering an unprecedented selection range of operating points in sub-$\mu$W levels for designers of ultralow power systems.

## OUTLOOK

We have integrated the suspended body of transistors into nanomechanical, single-crystalline silicon resonators operating at very high frequencies, ranging from 25 to 80 MHz. The electrostatic actuation and the transistor-based readout allow all-electronic actuation

and detection at room temperature. This solution can be extended to a very large scale integration with an SOI-CMOS compatible technology. The intrinsic gain mechanism of the n-type enhancement mode transistor improves the available signal-to-noise ratio and allows the performance of signal operations (mixing, amplification) equivalent to field effect transistors used in integrated circuitry, however, coupled with the tunable, highly selective spectral properties of mechanical resonators. We have observed mechanical resonances in weak inversion, opening a design space between gain and device power dissipation with access to record-low power consumption (nW). Further, the top-down surface nanomachining allows the high degree of freedom in the design of resonators itself, in contrast to bottom-up procedures. The resonator structure, modal shape, and operating frequencies, as well as transistor properties maybe be optimized toward a specific application. Finally, the RB-FinFET can fully benefit from even more aggressive scaling of the channel lengths in a similar way as its solid-state counterpart, and the reported charge modulation can be complemented by piezoresistive modulation, which offers new design opportunities for performance at nanoscale.

## METHODS

**Resonator Fabrication.** The fabrication combines two e-beam lithographic steps and two optical masks. The structures are fabricated on SOI wafers, with an initial 290 nm thick silicon (Si) device layer and a p-type resistivity of ~16 Ω cm . The thickness of the buried oxide is chosen to be 1 $\mu$m. A Boron implantation at 40 keV is performed and then activated by diffusion during a thermal oxidation process. A 100 nm wet oxide hard mask is grown, thinning the substrate down to 230 nm. The design of the structures is transferred to the silicon oxide layer with e-beam lithography at 5 nm resolution and subsequently transferred into the silicon device layer, exploiting a RIE process based on chlorine chemistry. A controlled notching effect is employed to obtain vertical sidewalls. After a wet release-etch in BHF and a supercritical point drying in $CO_2$, a 40 nm thermal oxide is grown, essentially thinning down the silicon to ~200 nm. A 500 nm low-stress LPCVD amorphous silicon, (a-)Si, layer is used as hard mask for the gate, source, and drain implantation. To obtain 50 nm precision alignments for high energy implantation, a second e-beam lithography step is required. The a-Si etch with bromine hydrate is particularly well suited for vertical etching on high aspect ratio structures. A phosphorus implantation is performed at 120 keV and activated by a rapid thermal annealing (RTA) to minimize any further diffusion. During the final metallization step, two optical masks are used, one for opening the gate oxide, etched in BHF in the contact region, and a second to pattern the 400 nm PVD aluminum layer using a two-layer lift-off process. Finally, the a-Si is removed by a fluorine-based isotropic dry Si etching and the metal annealed at 400 °C.

**Resonator Characterization.** The devices are located in a vacuum probe chamber (Süss Microtec PMC150) under high vacuum (~$10^{-5}$ mbar), and the electrical characterization was performed at room temperature (300 K). Care was taken to ensure the coherence of the resonant response with respect to device operating conditions. We then use an Agilent 4156C analyzer as the dc voltage source with mV step resolution and keep conditions of ac-drives, temperature, and chamber pressure constant. We have not observed any hysteretic behavior of the static characteristics in vacuum conditions. Direct transmission measurements were performed on the Agilent Vector Network Analyzer 8749. For mixer measurements, the intermediate frequency output is monitored with the Stanford Research Lock-in Amplifier SR830 or on an Agilent Spectrum Analyzer 89600S.

*Acknowledgment.* This work was supported by the European Framework Project FP7 NEMSIC "Hybrid Nano-Electro-Mechanical Systems for Sensing and Power Management Applications". We thank S. Ayöz for help in the measurement apparatus and A. Rusu for advice with customized data acquisition. We thank the staff of EPFL Centre for MicroNanotechnology (CMI) for assistance in device fabrication.

*Supporting Information Available:* Additional experimental details and figures. This material is available free of charge *via* the Internet at http://pubs.acs.org.

## REFERENCES AND NOTES

1. Nguyen, C. T. C. MEMS Technology for Timing and Frequency Control. *Proc. IEEE Int. Freq. Control Symp., 2005* **2005**, *1–11*, 955.
2. Abele, N.; Fritschi, R.; Boucart, K.; Casset, F.; Ancey, P.; Ionescu, A. M. Suspended-Gate MOSFET: Bringing New MEMS Functionality into Solid-State MOS Transistor. *Tech. Dig.—Int. Electron. Devices Meet.* **2005**, *1075—1077*, 1089.
3. Wong, A. C.; Nguyen, C. T. C. Micromechanical Mixer-Filters ("Mixlers"). *J. Microelectromech. Syst.* **2004**, *13*, 100–112.
4. Ekinci, K. L.; Huang, X. M. H.; Roukes, M. L. Ultrasensitive Nanoelectromechanical Mass Detection. *Appl. Phys. Lett.* **2004**, *84*, 4469–4471.
5. Mamin, H. J.; Rugar, D. Sub-attonewton Force Detection at Millikelvin Temperatures. *Appl. Phys. Lett.* **2001**, *79*, 3358–3360.
6. Knobel, R. G.; Cleland, A. N. Nanometre-Scale Displacement Sensing Using a Single Electron Transistor. *Nature* **2003**, *424*, 291–293.
7. O'Connell, A. D.; Hofheinz, M.; Ansmann, M.; Bialczak, R. C.; Lenander, M.; Lucero, E.; Neeley, M.; Sank, D.; Wang, H.; Weides, M.; et al. Quantum Ground State and Single-phonon Control of a Mechanical Resonator. *Nature* **2010**, *464*, 697–703.
8. Anetsberger, G.; Riviere, R.; Schliesser, A.; Arcizet, O.; Kippenberg, T. J. Ultralow-Dissipation Optomechanical Resonators on a Chip. *Nat. Photonics* **2008**, *2*, 627–633.
9. Teufel, J. D.; Donner, T.; Castellanos-Beltran, M. A.; Harlow, J. W.; Lehnert, K. W. Nanomechanical Motion Measured with an Imprecision Below that at the Standard Quantum Limit. *Nat. Nanotechnol.* **2009**, *4*, 820–823.
10. Li, M.; Tang, H. X.; Roukes, M. L. Ultra-Sensitive NEMS-based Cantilevers for Sensing, Scanned Probe and Very High-frequency Applications. *Nat. Nanotechnol.* **2007**, *2*, 114–120.
11. Cleland, A. N.; Roukes, M. L. Fabrication of High Frequency Nanometer Scale Mechanical Resonators from Bulk Si Crystals. *Appl. Phys. Lett.* **1996**, *69*, 2653–2655.
12. Karabalin, R. B.; Matheny, M. H.; Feng, X. L.; Defay, E.; Le Rhun, G.; Marcoux, C.; Hentz, S.; Andreucci, P.; Roukes, M. L. Piezoelectric Nanoelectromechanical Resonators Based on Aluminum Nitride Thin Films. *Appl. Phys. Lett.* **2009**, 95.
13. Azak, N. O.; Shagam, M. Y.; Karabacak, D. M.; Ekinci, K. L.; Kim, D. H.; Jang, D. Y. Nanomechanical Displacement Detection Using Fiber-Optic Interferometry. *Appl. Phys. Lett.* **2007**, 91.
14. Unterreithmeier, Q. P.; Faust, T.; Manus, S.; Kotthaus, J. P. On-Chip Interferometric Detection of Nanomechanical Motion. *Nano Lett.* **2010**, *10*, 887–890.
15. Li, M.; Pernice, W. H. P.; Tang, H. X. Broadband All-Photonic Transduction of Nanocantilevers. *Nat. Nanotechnol.* **2009**, *4*, 377–382.
16. Truitt, P. A.; Hertzberg, J. B.; Huang, C. C.; Ekinci, K. L.; Schwab, K. C. Efficient and Sensitive Capacitive Readout of Nanomechanical Resonator Arrays. *Nano Lett.* **2007**, *7*, 120–126.

17. Sampathkumar, A.; Ekinci, K. L.; Murray, T. W. Multiplexed Optical Operation of Distributed Nanoelectromechanical Systems Arrays. *Nano Lett.* **2011**, *11*, 1014–1019.
18. Sinha, N.; Wabiszewski, G. E.; Mahameed, R.; Felmetsger, V.; Tanner, S.; Carpick, R. W.; Piazza, G. Piezoelectric Aluminum Nitride Nanoelectromechanical Actuators. *Appl. Phys. Lett.* **2009**, 95.
19. Weinstein, D.; Bhave, S. A. The Resonant Body Transistor. *Nano Lett.* **2010**, *10*, 1234–1237.
20. van Beek, J. T. M.; Verheijden, G. J. A. M.; Koops, G. E. J.; Phan, K. L.; van der Avoort, C.; van Wingerden, J.; Badaroglu, D. E.; Bontemps, J. J. M. Scalable 1.1 GHz Fundamental Mode Piezo- Resistive Silicon MEMS Resonator. *Tech. Dig.—Int. Electron. Devices Meet.* **2010**, *411—414*, 1043.
21. He, R. R.; Feng, X. L.; Roukes, M. L.; Yang, P. D. Self-Transducing Silicon Nanowire Electromechanical Systems at Room Temperature. *Nano Lett.* **2008**, *8*, 1756–1761.
22. Mile, E.; Jourdan, G.; Bargatin, I.; Labarthe, S.; Marcoux, C.; Andreucci, P.; Hentz, S.; Kharrat, C.; Colinet, E.; Duraffourg, L. In-plane Nanoelectromechanical Resonators Based on Silicon Nanowire Piezoresistive Detection. *Nanotechnology* **2010**, 21.
23. Colinet, E.; Durand, C.; Duraffourg, L.; Audebert, P.; Dumas, G.; Casset, F.; Ollier, E.; Ancey, P.; Carpentier, J. F.; Buchaillot, L.; et al. Ultra-Sensitive Capacitive Detection Based on SGMOSFET Compatible With Front-End CMOS Process. *IEEE J. Solid-State Circuits* **2009**, *44*, 247–257.
24. Nathanso, Hc; Newell, W. E.; Wickstro, Ra; Davis, J. R. Resonant Gate Transistor. *IEEE Electron Dev.* **1967**, *Ed14*), 117.
25. Li, M.; Myers, E. B.; Tang, H. X.; Aldridge, S. J.; McCaig, H. C.; Whiting, J. J.; Simonson, R. J.; Lewis, N. S.; Roukes, M. L. Nanoelectromechanical Resonator Arrays for Ultrafast, Gas-Phase Chromatographic Chemical Analysis. *Nano Lett.* **2010**, *10*, 3899–3903.
26. Cheng, T. J.; Bhave, S. A. High-Q, Low Impedance Polysilicon Resonators with 10 Nm Air Gaps. *IEEE Int. Conf. Micro Electro Mech. Syst., Tech. Dig., 23rd* **2010**, *695—698*, 1210.
27. Coling, J.-P. *Silicon-On-Insulator Technology*; Kluwer Academic Publishers: Norwell, MA, 1997; pp 123—153.
28. Grogg, D.; Mazza, M.; Tsamados, D.; Ionescu, A. M. Multi-Gate Vibrating-Body Field Effect Transistor (VB-FETs). *Tech. Dig.—Int. Electron. Devices Meet.* **2008**, *663—666*, 949.
29. Cleland, A. N.; Roukes, M. L. A Nanometre-Scale Mechanical Electrometer. *Nature* **1998**, *392*, 160–162.
30. Knobel, R.; Yung, C. S.; Cleland, A. N. Single-Electron Transistor as a Radio-Frequency Mixer. *Appl. Phys. Lett.* **2002**, *81*, 532–534.
31. Kim, H. S.; Qin, H.; Blick, R. H. Direct Mechanical Mixing in a Nanoelectromechanical Diode. *Appl. Phys. Lett.* **2007**, 91.
32. Rodriguez-Morales, F.; Zannoni, R.; Nicholson, J.; Fischetti, M.; Yngvesson, K. S.; Appenzeller, J. Direct and Heterodyne Detection of Microwaves in a Metallic Single Wall Carbon Nanotube. *Appl. Phys. Lett.* **2006**, 89.
33. Rosenblatt, S.; Lin, H.; Sazonova, V.; Tiwari, S.; McEuen, P. L. Mixing at 50 GHz Using a Single- Walled Carbon Nanotube Transistor. *Appl. Phys. Lett.* **2005**, 87.
34. Pesetski, A. A.; Baumgardner, J. E.; Folk, E.; Przybysz, J. X.; Adam, J. D.; Zhang, H. Carbon Nanotube Field-Effect Transistor Operation at Microwave Frequencies. *Appl. Phys. Lett.* **2006**, 88.
35. Appenzeller, J.; Frank, D. J. Frequency Dependent Characterization of Transport Properties in Carbon Nanotube Transistors. *Appl. Phys. Lett.* **2004**, 84.
36. Pashkin, Y. A.; Li, T. F.; Pekola, J. P.; Astafiev, O.; Knyazev, D. A.; Hoehne, F.; Im, H.; Nakamura, Y.; Tsai, J. S. Detection of Mechanical Resonance of a Single-Electron Transistor by Direct Current. *Appl. Phys. Lett.* **2010**, 96.
37. Sazonova, V.; Yaish, Y.; Ustunel, H.; Roundy, D.; Arias, T. A.; McEuen, P. L. A Tunable Carbon Nanotube Electromechanical Oscillator. *Nature* **2004**, *431*, 284–287.
38. Chen, C. Y.; Rosenblatt, S.; Bolotin, K. I.; Kalb, W.; Kim, P.; Kymissis, I.; Stormer, H. L.; Heinz, T. F.; Hone, J. Performance of Monolayer Graphene Nanomechanical Resonators with Electrical Readout. *Nat. Nanotechnol.* **2009**, *4*, 861–867.
39. Gouttenoire, V.; Barois, T.; Perisanu, S.; Leclercq, J. L.; Purcell, S. T.; Vincent, P.; Ayari, A. Digital and FM Demodulation of a Doubly Clamped Single-Walled Carbon-Nanotube Oscillator: Towards a Nanotube Cell Phone. *Small* **2010**, *6*, 1060–1065.
40. Maas, S. A. A Gaas-Mesfet Mixer with Very Low Intermodulation. *IEEE Trans. Microwave Theory Tech.* **1987**, *35*, 425–429.
41. Huttel, A. K.; Steele, G. A.; Witkamp, B.; Poot, M.; Kouwenhoven, L. P.; van der Zant, H. S. J. Carbon Nanotubes as Ultrahigh Quality Factor Mechanical Resonators. *Nano Lett.* **2009**, *9*, 2547–2552.
42. Rutherglen, C.; Burke, P. Carbon Nanotube Radio. *Nano Lett.* **2007**, *7*, 3296–3299.
43. Hsu, W. T.; Clark, J. R.; Nguyen, C. T. C. Mechanically Temperature-Compensated Flexural- Mode Micromechanical Resonators. *Tech. Dig.—Int. Electron. Devices Meet.* **2000**, 399–402.
44. Szekeres, A.; Danesh, P. Mechanical Stress in SiO2/Si Structures Formed by Thermal Oxidation of Amorphous and Crystalline Silicon. *Semicond. Sci. Technol.* **1996**, *11*, 1225–1230.
45. Bhiladvala, R. B.; Wang, Z. J. Effect of Fluids on the Q Factor and Resonance Frequency of Oscillating Micrometer and Nanometer Scale Beams. *Phys. Rev. E* **2004**, 69.
46. Li, M.; Bhiladvala, R. B.; Morrow, T. J.; Sioss, J. A.; Lew, K.; Redwing, J. M.; Keating, C. D.; Mayer, T. S. Bottom-Up Assembly of Large-Area Nanowire Resonator Arrays, Nat. *Nanotechnology* **2008**, *3*, 88–92.
47. Sze, S. M. *Phys. Semicond. Dev.* **2007**, 293–320.
48. Wacker, N.; Richter, H.; Hassan, M. U.; Rempp, H.; Burghartz, J. N. Compact Modeling of CMOS Transistors under Variable Uniaxial Stress. *Solid-State Electron.* **2011**, *57*, 52–60.
49. Bartsch, S. T.; Grogg, D.; Lovera, A.; Tsamados, D.; Ayoz, S.; Ionescu, A. M. Resonant-Body Fin-FETs with sub-nW Power Consumption. *Tech. Dig.—Int. Electron. Devices Meet.* **2010**, 761–764.